2015-03-01

Creep cavitation bands control porosity and fluid flow in lower crustal shear zones

Menegon, L

10.1130/G36307.1
Geology

Geology

Creep cavitation bands control porosity and fluid flow in lower crustal shear zones

--Manuscript Draft--

Manuscript Number:	G36307R1
Full Title:	Creep cavitation bands control porosity and fluid flow in lower crustal shear zones
Short Title:	Creep cavitation bands in lower crustal shear zones
Article Type:	Article
Keywords:	creep cavitation; diffusion creep; grain boundary sliding; fluid flow; shear zone rheology; lower crust.
Corresponding Author:	Luca Menegon Plymouth University, UK Plymouth, Devon UNITED KINGDOM
Corresponding Author Secondary Information:	
Corresponding Author's Institution:	Plymouth University, UK
Corresponding Author's Secondary Institution:	
First Author:	Luca Menegon
First Author Secondary Information:	
Order of Authors:	Luca Menegon
	Florian Fusseis
	Holger Stünitz
	Xianghui Xiao
Order of Authors Secondary Information:	
Manuscript Region of Origin:	NORWAY
Abstract:	Shear zones channelize fluid flow in the Earth's crust. However, little is known about deep crustal fluid migration and how fluids are channelized and distributed in a deforming lower crustal shear zone. This study investigates the deformation mechanisms, fluid-rock interaction and development of porosity in a monzonite ultramylonite from Lofoten, northern Norway. The rock was deformed and transformed into an ultramylonite under lower crustal conditions (T=700-730° C, P=0.65-0.8 GPa). The ultramylonite consists of feldspathic layers and domains of amphibole + quartz + calcite, which result from hydration reactions of magmatic clinopyroxene. The average grain size in both domains is <25 m. Microstructural observations and EBSD analysis are consistent with diffusion creep as the dominant deformation mechanism in both domains. Festoons of isolated quartz grains define C'-type shear bands in feldspathic layers. These quartz grains do not show a crystallographic preferred orientation. The alignment of quartz grains is parallel to the preferred elongation of pores in the ultramylonites, as evidenced from synchrotron X-ray microtomography. Such C'-type shear bands are interpreted as creep cavitation bands resulting from diffusion creep deformation associated with grain boundary sliding. Mass-balance calculation indicates a 2% volume increase during the protolith-ultramylonite transformation, which is consistent with synkinematic formation of creep cavities producing dilatancy. Thus, this study presents evidence that creep cavitation bands may control deep crustal porosity and fluid flow. Nucleation of new phases in creep cavitation bands inhibits grain growth and enhances the activity of grain-size sensitive creep, thereby stabilising strain localization in the polymineralic ultramylonites.
Response to Reviewers:	Please see attached cover letter. Best wishes, Luca Menegon

Creep cavitation bands control porosity and fluid flow in lower crustal shear zones

Luca Menegon[1], Florian Fusseis[2], Holger Stünitz[3], and Xianghui Xiao[4]

[1]*School of Geography, Earth and Environmental Sciences, Plymouth University, Plymouth, PL4 8AA, United Kingdom*

[2]*School of Geosciences, University of Edinburgh, Edinburgh, EH9 3FE, United Kingdom*

[3] *Department of Geology, University of Tromsø, 9037 Tromsø, Norway*

[4] *Advanced Photon Source, Argonne National Laboratory, Argonne, Illinois 60439, USA*

ABSTRACT

Shear zones channelize fluid flow in the Earth's crust. However, little is known about deep crustal fluid migration and how fluids are channelized and distributed in a deforming lower crustal shear zone. This study investigates the deformation mechanisms, fluid-rock interaction and development of porosity in a monzonite ultramylonite from Lofoten, northern Norway. The rock was deformed and transformed into an ultramylonite under lower crustal conditions (T=700-730° C, P=0.65-0.8 GPa). The ultramylonite consists of feldspathic layers and domains of amphibole + quartz + calcite, which result from hydration reactions of magmatic clinopyroxene. The average grain size in both domains is <25 μm. Microstructural observations and EBSD analysis are consistent with diffusion creep as the dominant deformation mechanism in both domains. Festoons of isolated quartz grains define C'-type shear bands in feldspathic layers. These quartz grains do not show a crystallographic preferred orientation. The alignment of quartz grains is parallel to the preferred elongation of pores in the ultramylonites, as evidenced from synchrotron X-ray microtomography. Such C'-type shear bands are interpreted as creep

cavitation bands resulting from diffusion creep deformation associated with grain boundary sliding. Mass-balance calculation indicates a 2% volume increase during the protolith-ultramylonite transformation, which is consistent with synkinematic formation of creep cavities producing dilatancy. Thus, this study presents evidence that creep cavitation bands may control deep crustal porosity and fluid flow. Nucleation of new phases in creep cavitation bands inhibits grain growth and enhances the activity of grain-size sensitive creep, thereby stabilising strain localization in the polymineralic ultramylonites.

INTRODUCTION

Many studies document that metamorphic reactions and viscous deformation in the lower crust are triggered by grain-size reduction and fluid infiltration (e.g., Austrheim, 1987; Rutter and Brodie 1992; Getsinger et al., 2013). A very fine grain size of reaction products may activate grain size sensitive creep, which leads to a marked weakening of the rock and to strain localization (Rutter and Brodie 1992; Pearce et al., 2011). The feedback between grain size reduction, fluid flow, and the activity of different deformation mechanisms is critical for the understanding of the rheology of shear zones and the processes leading to strain localization.

Deformation-enhanced fluid flow and development of synkinematic porosity in mid-crustal shear zones rocks has been a subject of numerous studies (e.g. Mancktelow et al., 1998; Fusseis et al., 2009). Fluid transfer has been linked to syndeformational dynamic porosity generated by creep cavitation during viscous grain boundary sliding (e.g., the granular fluid pump model: Fusseis et al., 2009). Fluid infiltration results in shear zones being preferential conduits for fluid flow even at deeper crustal conditions (Austrheim, 1987; Mancktelow, 2006). However, little is known about the fluid flow in the lower crust, and, more specifically, about the processes that control formation and distribution of syndeformational porosity.

High strain torsion experiments on synthetic anorthite aggregates deforming by grain boundary sliding have highlighted the development of creep cavitation bands (Rybacki et al., 2008; 2010). The bands developed with a C'-type shear band orientation, presumably from growth and coalescence of individual pores originally formed at triple junctions and dilatant sites resulting from the operation of grain boundary sliding. However, observational evidence of similar creep cavitation bands in natural ultramylonites from the lower crust is currently lacking, thus questioning the extrapolation of such experimental results to natural conditions.

To investigate the relationships between deformation mechanisms and the formation and distribution of porosity in lower crustal shear zones, we have analysed a feldspar-rich ultramylonite deformed at T>700° C. Our results provide evidence for the formation of creep cavitation bands during grain-size sensitive creep and have important implications for the understanding of high-temperature creep and synkinematic fluid flow in the lower crust.

SAMPLES AND METHODS

We sampled a shear zone in the Anorthosite-Monzonite-Charnockite-Granite intrusive suite of Lofoten, northern Norway (Corfu, 2004, and references therein). The shear zone is hosted in monzonite and shows a mylonite to ultramylonite transition from the shear zone boundary to the shear zone centre (see Fig. DR1; sample location in UTM coordinates relative to WGS84: zone 33W, 0505656E, 7594514N). The transition is marked by an extreme grain size reduction of perthites and clinopyroxene. Grain size reduction occurred by fracturing and neocrystallization in perthites and by hydration reactions in clinopyroxene, forming amphibole + quartz + calcite. Plagioclase-amphibole geothermobarometry and Ti-in-amphibole geothermometry yield P, T conditions of deformation of 700-730° C, 0.65-0.8 GPa (Menegon et al., 2013).

69 We used a combination of detailed microstructural analysis, synchrotron X-ray
70 microtomography and mass-balance calculations to characterize deformation microstructures and
71 the associated synkinematic porosity in the ultramylonite. Electron backscatter diffraction
72 (EBSD) was used to quantify the crystallographic preferred orientation (CPO) of feldspars,
73 amphibole and quartz. Analytical methods are described in detail in the Data Repository.

74 **RESULTS**

75 **Microstructure and EBSD analysis**

76 The ultramylonite displays a compositional banding between feldspathic layers and
77 domains of pyroxene-derived reaction products (amphibole, quartz and calcite) (Fig. 1A). The
78 feldspathic layers originate from the neocrystallization of perthites, and may locally contain also
79 quartz, amphibole and biotite (Fig. 1B). The rare clinopyroxene porphyroclasts preserved in the
80 ultramylonite show the localization of reaction products along intragranular fractures (Fig. 1C).
81 Calcite is a synkinematic reaction product, typically at triple junctions and dilatant sites (Fig.
82 1D). In both feldspathic and pyroxene-derived domains the average grain size is < 25 μm.

83 The EBSD phase map of a feldspathic layer shown in Fig. 2A is dominated by the bi-
84 phase mixture of plagioclase and K-feldspar deriving from the recrystallization of original
85 perthites. The EDS compositional map of the Si content of the same area is shown in Fig. 2B.
86 Quartz occurs as isolated grains along discrete C'-bands inclined at 10-20° to the trace of the
87 ultramylonite foliation, consistent with the sinistral sense of shear (Fig. 2A, 2B). The CPO of
88 quartz, K-feldspar and plagioclase and does not show a clear relationship of crystallographic
89 planes and axes with the kinematic framework of the ultramylonite (Fig. 2C). The long axis of
90 quartz grains are preferentially oriented either at 0-40° or at 160-180° to the trace of the
91 ultramylonite foliation, measured anticlockwise (Fig. 2D). An additional EBSD map of a

92 feldspathic layer containing festoons of quartz grains in a C'-band orientation is shown in the
93 supplementary material (Fig. DR2).
94 Amphibole CPO in an elongate domain of reaction products shows clusters of [001] axes
95 oriented at a low angle to the stretching lineation. Poles to the (100) and (010) planes are
96 preferentially distributed along a girdle subparallel to the YZ plane (Fig. 2E). In the same
97 domain, quartz c-axis CPO is weak and characterized by some clustering at a low angle to the
98 foliation plane. One cluster occurs near the centre of the pole figure (Fig. 2E).
99 **Porosity distribution and orientation**
100 We used synchrotron X-ray microtomography to analyse the distribution and orientation
101 of pores in two feldspathic layers that were micro-drilled from the ultramylonite sample (Fig.
102 3A; see GSA Data Repository for details on data acquisition). The absorption microtomographic
103 data resolve the different materials in the sample well and clearly highlight the pores, which
104 attenuate the least and appear darkest (yellow in Fig. 3A; movies DR_ Lu-
105 1_light_pores_slcmigration and DR_ Lu-3_light_pores_slcmigration in the Data Repository).
106 Low-aspect-ratio-pores can easily be distinguished from cracks that might have formed
107 along grain boundaries during exhumation and cooling of the rocks (movie Lu-
108 1_pores_slcmigration_1). The latter were excluded from the following analyses. Although pore
109 diameters can vary from about the resolution limit (1.5 μm diameter) to about 20 μm, they
110 generally are significantly smaller than the grains themselves. The pores decorate phase and
111 grain boundaries between feldspars and quartz, hornblende and/or biotite and often form festoons
112 or clusters of more than two pores.
113 Pores were segmented by binary thresholding and analysed for their orientations.
114 Orientation of each pore was defined as the orientation of the best ellipsoid fit to the pore's

115 shape. To avoid a bias in the orientation data, the analysis was limited to pores with volumes
116 between 34 μm^3 (125 voxels) and 4119 μm^3 ($1.5x10^4$ voxels). In figure 3 we show the results
117 from one feldspathic layer (data-set Lu-3_light); similar results were obtained from the second
118 feldspathic layer (data-set Lu-1_light: see Fig. DR3). The pole figure shows the orientation of the
119 long axis of the best-fit ellipsoid of the pores. These are referenced to the trace of the mylonitic
120 foliation (a kinematic framework defined by the long axis of the best ellipsoid fit to the biotite
121 grains, Fig. 3B). The diagram reveals that the pores have a preferred orientation, with their long
122 axes oriented at 20-30° to the trace of the mylonitic foliation, in a C'-band orientation (Fig. 3B).

123 **Mass-balance calculations**

124 Whole-rock chemistry and total carbon (TC) analysis was performed to assess element
125 mobility and volume changes during the protolith-to-ultramlyonite transformation using the
126 'normalized Gresens' method (Potdevin and Marquer, 1987). Results of the whole-rock
127 chemistry analysis are reported in Table DR1.

128 The total carbon (TC) content of the ultramylonite is 2.75 times higher than the original
129 content in the protolith (0.139 Vs. 0.037 wt%). Assuming that the original monzonite contained
130 minute amounts of carbonate material, we used TC as a reference to calculate the volume change
131 associated with the shear zone formation. The TC increase reflects CO_2 infiltration during
132 shearing, consistent with the synkinematic growth of calcite in the ultramylonite (Figs. 1C, 1D).
133 A 2.75 times increase of TC implies a volume increase of 2.3%. Detailed information on the
134 mass-balance results is compiled in the Data Repository.

135 **DISCUSSION**

136 The CPO of all phases, the grain size and shape, and phase mixing indicate that grain size
137 sensitive creep was the dominant deformation mechanism in both, the feldspathic layers and the

pyroxene-derived layers in the ultramylonite. The feldspar CPO data is not interpretable in terms of intracrystalline plasticity. In the layers composed of reaction products, the similar grain sizes and shapes of calcite, quartz and hornblende indicate the dominance of grain size sensitive creep (Getsinger et al., 2013). At the given temperatures, calcite is expected to be substantially weaker than quartz and hornblende if deforming by dislocation creep (e.g., Renner et al., 2007). However, in the microstructures calcite never appears less competent, and all three phases show similar aspect ratios and grain sizes (Fig 1D). The distribution of hornblende [001] axes near the instantaneous stretching axis for a sinistral sense of shear (Fig. 2C) is consistent with a shape fabric attained by oriented growth and/or rigid body rotation during deformation accommodated by diffusion creep and grain boundary sliding, which is a common feature in amphibole deforming at lower crustal conditions (e.g., Berger and Stünitz, 1996; Getsinger and Hirth, 2014). Quartz c-axes show weak maxima oriented similar to hornblende [001] axes. We likewise interpret this weak CPO as the result of preferential synkinematic growth of quartz grains with their c-axis parallel to the elongation direction during diffusion creep (e.g. Hippertt, 1994; Hippertt and Egydio-Silva, 1996; Kilian et al., 2011).

The occurrence of quartz grains in a C'-band orientation in the feldspathic layers is interpreted as the result of creep cavitation, which is referred to as the coalescence of intergranular pores originally formed at grain triple junctions and grain boundaries (Zavada et al., 2007; Rybacki et al., 2008, 2010; Delle Piane et al., 2009). Creep cavitation takes place during grain boundary sliding, and dilating creep cavities form local sites of low stress that attract grain boundary fluids (Fusseis et al., 2009). Our mass-balance calculations indicate (1) a volume increase of 2.3%, and (2) fluid infiltration during the protolith-ultramylonite transformation. Hence, positive volume change accompanied by fluid infiltration can explain the

precipitation of new phases from intragranular aqueous fluids collected in cavitation bands. Volume increase is a consequence of dilatancy at grain boundaries (Schmocker et al., 2003; Fusseis et al., 2009).

Our interpretation is supported by the similar orientation of the preferred elongation of pores in the feldspathic layers and the orientation of the C´ bands (Figs. 2A-B and 3). The orientation of pores is not related to specific phase boundaries but to the kinematic framework of the shear zone. Thus, we interpret the final porosity imaged by X-ray microtomography as representative of the porosity and fluid flow at an instant during deformation. The preferred distribution of pores and isolated quartz grains in a C'-type shear band orientation is a syndeformational feature reflecting the local dilatancy in a dynamically evolving microstructure during diffusion creep deformation (Schmocker et al., 2003; Rybacki et al. 2008, 2010). Grain boundary sliding, creep cavitation, and heterogeneous nucleation form pores or new grains in low stress sites (Ree 1994; Kassner and Hayes, 2003; Kilian et al., 2011) (Fig. 4). Dilatancy has an initial form normal to the extension direction and only after some extension and further opening of the porosity pore shape attains a stable orientation along C'-bands (Fig. 4).

The precipitation of quartz along dilatant grain boundaries requires material transport, most likely in a grain boundary fluid film. The interpretation is that quartz is dissolved from the pyroxene-derived reaction products (Fig. 1C) and precipitates locally in dilatant sites in the feldspathic layers. Dissolution, transport, grain rotation, and precipitation are intimately related processes during diffusion creep of geological material (e.g. Fusseis et al., 2009; Kilian et al., 2011), and may result in a dynamically evolving microstructure and distribution of porosity.

There is a certain degree of similarity between shape of pores and quartz grains. About 50% of the quartz grains contained in the festoons in Figs. 2A-B are preferentially elongated at 0-40°

184 to the trace of the foliation, similar to the elongation of pores (Figs. 2D, 3B). It could indicate
185 that shape of quartz grains is determined by the cavitation process (Fig. 4). However, considering
186 the shape modifications that quartz grains can undergo after precipitation (i.e. dissolution, grain
187 rotation), this is a speculation.

188 **IMPLICATIONS AND CONCLUSIONS**

189 We conclude that the orientations of pores, quartz bands and phase boundaries along C'-type
190 shear bands in the ultramylonite are evidence of creep cavitation during lower crustal
191 deformation accommodated by diffusion creep, grain boundary sliding and heterogeneous
192 nucleation. The microstructures presented in this paper share many similarities with the creep
193 cavitation bands reported from experimental deformation of synthetic anorthite aggregates
194 (Rybacki et al., 2008; 2010). Creep cavitation bands can be identified by the occurrence of pores
195 and isolated grains of different phases. However, if the same phases precipitate, this will result in
196 overgrowths on existing grains, thereby rendering the identification of dilatancy and cavitation
197 bands difficult.

198 Strain localization in lower crustal rocks is typically associated with grain size reduction,
199 hydration reactions and phase mixing (e.g., Rutter and Brodie, 1992; Pearce et al., 2011;
200 Getsinger et al., 2013). Phase mixing by heterogeneous nucleation during grain size sensitive
201 creep critically relies on synkinematic porosity (e.g., Hiraga et al., 2013). Creep cavitation can be
202 a major contributor to porosity in lower crustal shear zones, and hence control fluid flow.
203 Nucleation of new phases in cavitation bands inhibits grain growth and enhances the activity of
204 grain-size sensitive creep, thereby maintaining strain localized in the polymineralic ultramylonite
205 (e.g., Herwegh et al., 2011). Thus, our findings provide a key component for the understanding

206 of strain localization in the lower crust and of the mechanisms by which fluid flow can be
207 channelized within lower crustal shear zones.

208 **ACKNOWLEDGMENTS**

209 This work was funded by a grant from the Mohn Foundation (University of Tromsø) and by
210 Plymouth University. We thank Marianne Ahlbom, Natasha Stephen, Erling Ravna, and Trine
211 Dahl for their help with the EBSD, XRF, LOI and LECO analysis. We thank N. Mancktelow, S.
212 Piazolo and an anonymous reviewer for their constructive reviews. Use of the Advanced Photon
213 Source at Argonne National Laboratory was supported by the U.S. Department of Energy, Office
214 of Science, Office of Basic Energy Sciences, under Contract No. DE-AC02-06CH11357.

215 **REFERENCES CITED**

216 Austrheim, H., 1987, Eclogitization of lower crustal granulites by fluid migration through shear
217 zones: Earth and Planetary Science Letters, v. 81, p. 221-232, doi:10.1016/0012-
218 821X(87)90158-0.

219 Berger, A., Stunitz, H., 1996, Deformation mechanisms and reaction of hornblende: Examples
220 form the Bergell Tonalite (Central Alps): Tectonophysics, v. 257, p. 149-174,
221 doi:10.1016/0040-1951(95)00125-5.

222 Corfu, F., 2004, U-Pb age, setting and tectonic significance of the Anorthosite-Mangerite-
223 Charnockite-Granite suite, Lofoten-Vesterålen, Norway: Journal of Petrology, v. 45, p.
224 1799-1819, doi:10.1093/petrology/egh034.

225 Delle Piane, C., Wilson, C.J.L., Burlini, L., 2009, Dilatant plasticity in high-strain experiments
226 on calcite-muscovite aggregates: Journal of Structural Geology, v. 31, p. 1084-1099,
227 doi:10.1016/j.jsg.2009.03.005.

228 Fusseis, F., Regenauer-Lieb, K., Liu, J., Hough, R.M., and De Carlo, F., 2009, Creep cavitation
229 can establish a dynamic granular fluid pump in ductile shear zones: Nature, v. 459, p. 974-
230 977, doi: 10.1038/nature08051.
231 Getsinger, A.J., and Hirth, G., 2014, Amphibole fabric formation during diffusion creep and the
232 rheology of shear zones: Geology, v. 42, p. 535-538, doi:10.1130/G35327.1.
233 Getsinger, A.J., Hirth, G., Stünitz, H., and Goergen, E.T., 2013, Influence of water on the
234 rheology and strain localization in the lower continental crust: Geochemistry Geophysics
235 Geosystems, v. 14, p. 2247-2264, doi:10.1002/ggge.20148.
236 Herwegh, M., Linckens, J., Ebert, A., Berger, A., Brodhag, S.H., 2011, The role of second
237 phases for controlling microstructural evolution in polymineralic rocks: A review: Journal of
238 Structural Geology, v. 33, p. 1728-1750, doi:10.1016/j.jsg.2011.08.011.
239 Hippertt, J.F., 1994, Microstructures and *c*-axis fabrics indicative of quartz dissolution in sheared
240 quartzites and phyllonites: Tectonophysics, v. 229, 141-163.
241 Hippertt, J.F., Egydio-Silva M., 1996, New polygonal grains formed by dissolution redeposition
242 in quartz mylonite: Journal of Structural Geology, v. 18, p. 1345-1352.
243 Hiraga, T., Miyazaki, T., Yoshida, H., and Zimmerman, M.E., 2013, Comparison of
244 microstructures in superplastically deformed synthetic materials and natural mylonites:
245 mineral aggregation via grain boundary sliding: Geology, v. 41, p. 959-962.
246 Kassner, M.E., and Hayes, T.A., 2003, Creep cavitation in metals: International Journal of
247 Plasticity, v. 19, p. 1715-1748, doi:10.1016/S0749-6419(02)00111-0.
248 Kilian, R., Heilbronner, R., and Stünitz, H., 2011, Quartz grain size reduction in a granitoid rock
249 and the transition from dislocation to diffusion creep: Journal of Structural Geology, v. 33,
250 p. 1265-1284, doi:10.1016/j.jsg.2011.05.004.

Mancktelow, N.S., 2006, How ductile are ductile shear zones?: Geology, v. 34, p. 345-348.

Mancktelow, N.S., Grujic, D., Johnson, E.L., 1998, An SEM study of porosity and grain boundary microstructure in quartz mylonites, Simplon Fault Zone, Central Alps: Contributions to Mineralogy and Petrology, v. 131, p. 71-85.

Menegon, L., Stünitz, H., Nasipuri, P., Heilbronner, R., and Svahnberg, H., 2013, Transition from fracturing to viscous flow in granulite facies perthitic feldspar (Lofoten, Norway): Journal of Structural Geology, v. 48, p. 95-112, doi:10.1016/j.jsg.2012.12.004.

Pearce, M.A., Wheeler, J., and Prior, D.J., 2011, Relative strength of mafic and felsic rocks during amphibolite facies metamorphism and deformation: Journal of Structural Geology, v. 33, p. 662-675, doi:10.1016/j.jsg.2011.01.002.

Pilling, J., and Ridley, N., 1989, Superplasticity in crystalline solids: The Institute of Metals, London, 214 pp.

Potdevin, J.L., and Marquer, D., 1987, Méthodes de quantification des transferts de matière par les fluides dans les roches métamorphiques déformées: Geodinamica Acta, v. 1, p. 193-206.

Ree, J.-H., 1994, Grain boundary sliding and development of grain boundary openings in experimentally deformed octalchloropropane: Journal of Structural Geology, v. 16, p. 403-418, doi:10.1016/0191-8141(94)90044-2.

Renner, J., Siddiqi, G., and Evans, B., 2007, Plastic flow of two-phase marbles: Journal of Geophysical Research, v. 112, B07203, doi:10.129/2005JB004134.

Rutter, E.H., and Brodie, K.H., 1992, Rheology of the lower crust, *in* Fountain, D.M., Arculus, R., and Yay, R.W., eds., Continental Lower Crust: Elsevier, Amsterdam, p. 201-267.

Rybacki, E., Wirth, R., and Dresen, G., 2008, High-strain creep of feldspar rocks: Implications for cavitation and ductile failure in the lower crust: Geophysical Research Letters, v. 35, L04304, doi: 10.1029/2007GL032478.

Rybacki, E., Wirth, R., and Dresen, G., 2010, Superplasticity and ductile fracture of synthetic feldspar deformed to large strain: Journal of Geophysical Research, v. 115, B08209, doi: 1029/2009JB007203.

Schmocker, M., Bystricky, M., Kunze, K., Burlini, L., Stunitz, H., Burg, J.-P., 2003, Granular flow and Riedel band formation in water rich quartz aggregates deformed in torsion: Journal of Geophysical Research, v. 108, p. 2242, doi:10.1029/2002JB001958.

Zavada, P., Schulmann, K., Konopásek, J., Ulrich, S, and Lexa, O., 2007, Extreme ductility of feldspar aggregates – Melt-enhanced grain boundary sliding and creep failure: Rheological implications for felsic lower crust: Journal of Geophysical Research, v. 112, B10210, doi:10.1029/2006JB004820.

FIGURE CAPTIONS

Figure 1. Microstructure of the ultramylonite in thin sections cut normal to foliation and parallel to stretching lineation. Abbreviations: FL=feldspathic layer, PDRP=pyroxene-derived reaction products, Pl=plagioclase, Kfs=K-feldspar, Qtz=quartz, Hbl=hornblende, Cpx=clinopyroxene, Cc=calcite, Bt=biotite. A: Light micrograph of the layered microstructure of the ultramylonite. Parallel polarizer. B: SEM backscattered electron image of a feldspathic layer. C: SEM backscattered electron image of pyroxene-derived reaction products. Note the clinopyroxene porphyroclast with reaction products along intracrystalline fractures. D: Close-up of pyroxene-derived reaction products. SEM backscattered electron image.

294 Figure 2. Results of EBSD and EDS analysis of the ultramylonite. All plots are upper
295 hemisphere projections contoured with 15° half-width and 5° cluster size using Channel 5
296 (Oxford Instruments). Inset in C shows the kinematic framework of the sample (L_s=stretching
297 lineation). Data is plotted as one point per grain (N = number of plotted grains). Maxima are
298 expressed as multiples of the uniform distribution. Mean angular deviation number for all
299 datasets is < 0.9. Shear sense is sinistral. A: Processed EBSD phase map from a feldspathic layer.
300 The map is superposed to the band contrast map. Grey areas are non-indexed points. Mineral
301 abbreviations: Kfs=K-feldspar, Pl=plagioclase, Qtz=quartz, Cc=calcite, Bt=biotite, Grt=garnet.
302 B: EDS-derived compositional map of Si content of the same area shown in A. C: Pole figures of
303 the crystallographic orientation data of quartz, K-feldspar and plagioclase from the area shown in
304 A. D: Rose diagram to show the orientation of the long axis of quartz grains included in A. Only
305 grains with aspect ratio > 1.3 are considered (N=50). E: Pole figures of the crystallographic
306 orientation data of hornblende and quartz from a layer of pyroxene-derived reaction products.
307 Figure 3. Synchrotron x-ray microtomographic data. S is the trace of the ultramylonite foliation,
308 C' the trace of C'-bands, L_s the stretching lineation (red dot). A: Slice through microtomographic
309 data Lu-3_light, showing 3D objects in 2D. Grey values correspond to x-ray absorption.
310 Red=biotite, yellow=pores. The grey-scale image is the backside of a thin migrating box through
311 the 3D data-set, in which pores and biotite are highlighted. As the box moves through the
312 volume, pores and biotite disappear out of the box at the front and enter the slice at the back,
313 through the greyscale image (see movie DR_Lu-3_light_pores_slcmigration in the Data
314 Repository). The inset shows the trends of preferred orientation of pores and biotite. B: Pole
315 figure illustrating the long axes of pores preferentially oriented at 20-30° to the foliation (top)
316 and the preferred orientation of biotite long axis aligned in the foliation plane (bottom). Data is

plotted as one-point-per-pore (or biotite) and as contoured pole figures. Equal area lower hemisphere stereoplots. Contouring is up to 10 times MUD.

Figure 4. Schematic drawing of cavitation during grain boundary sliding in shear (after Pilling and Ridley 1989). Elongation orientation of the pores will depend on the extent of dilatancy.

[1]GSA Data Repository item 2014xxx, xxxxxxxx, is available online at www.geosociety.org/pubs/ft2014.htm, or on request from editing@geosociety.org or Documents Secretary, GSA, P.O. Box 9140, Boulder, CO 80301, USA.

Figure 1

Click here to download Figure: Fig1_microstructure.pdf

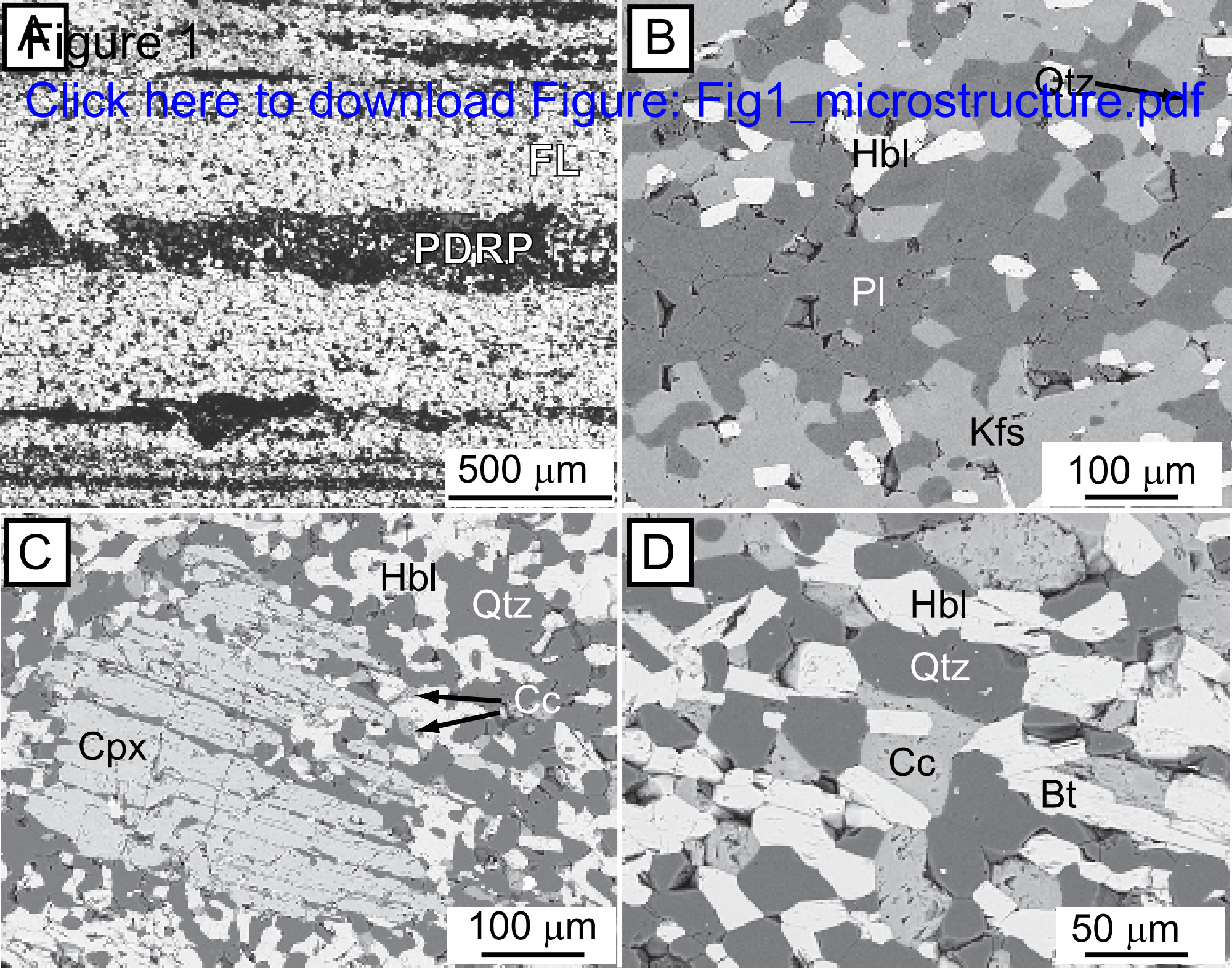

Fig. 1

Figure 2

Click here to download Figure: Fig2_EBSD_new.pdf

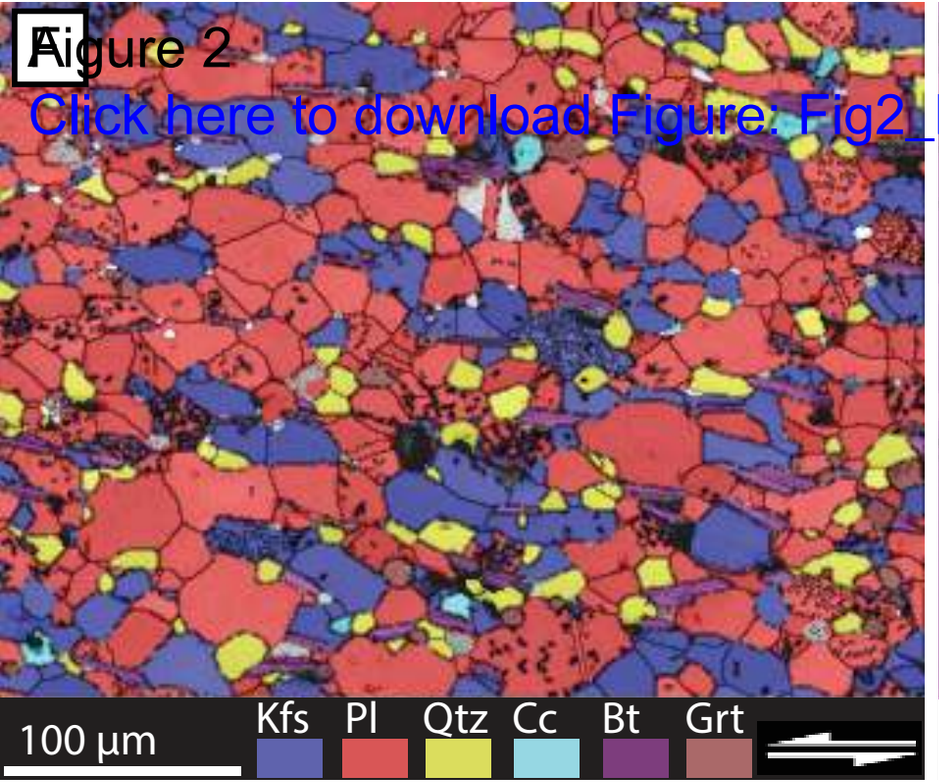

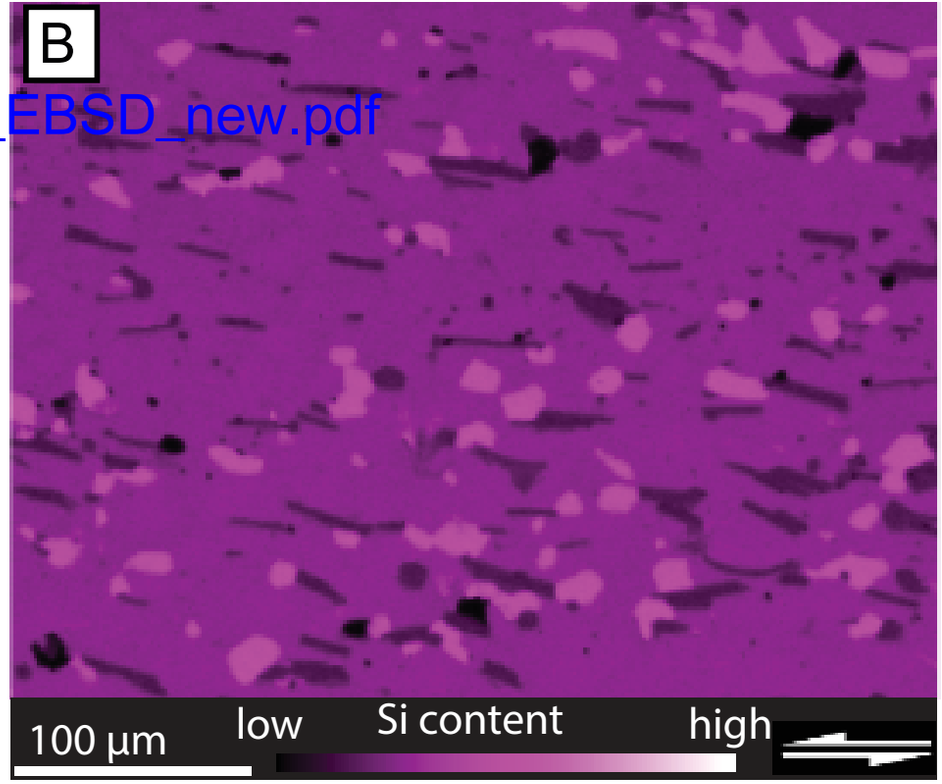

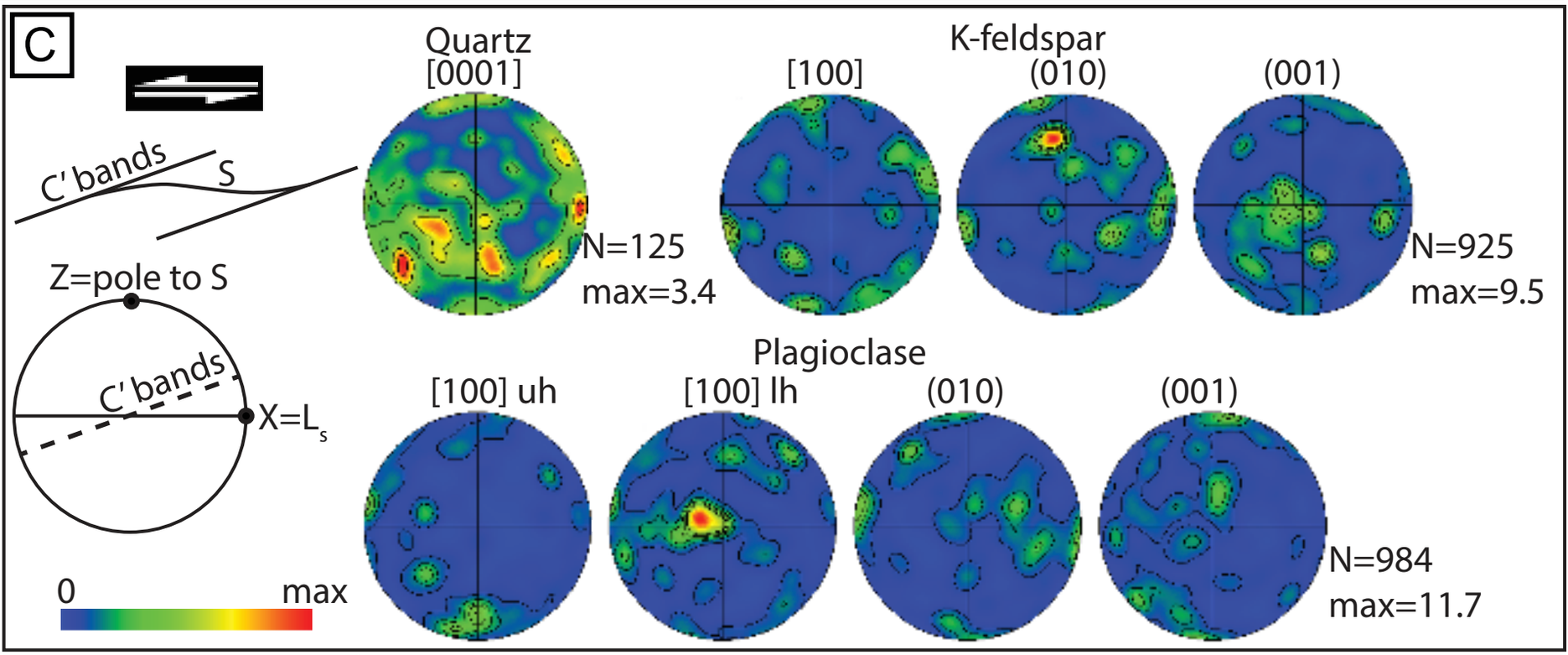

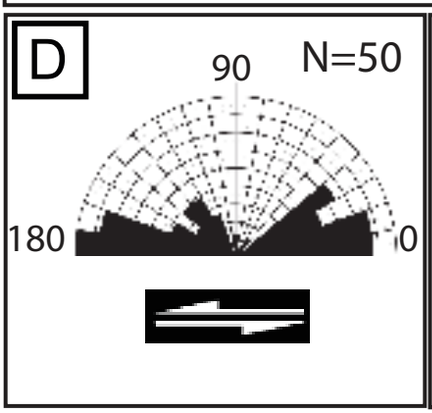

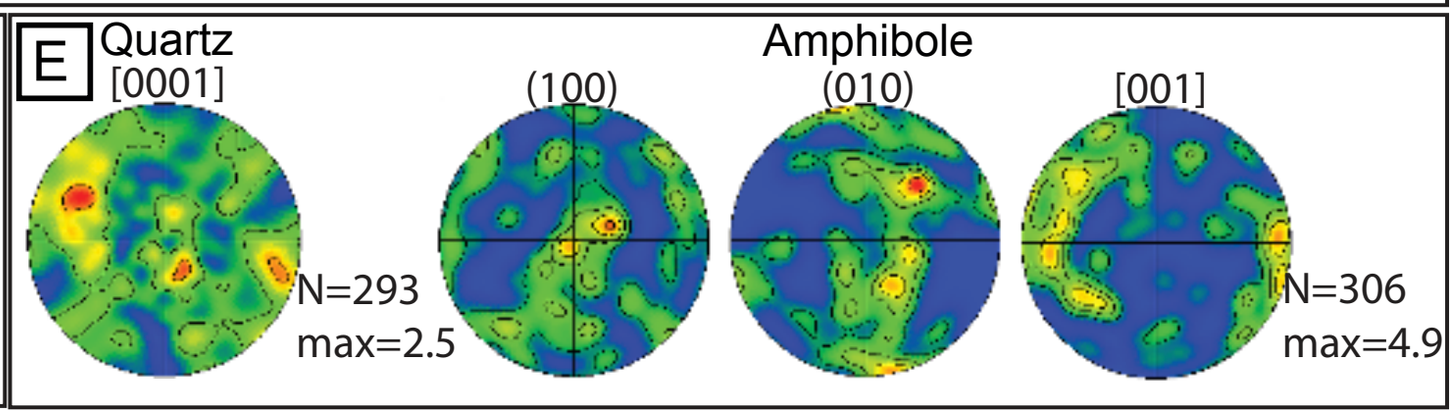

Figure 3

Click here to download Figure: Fig3_microtomography_new.pdf

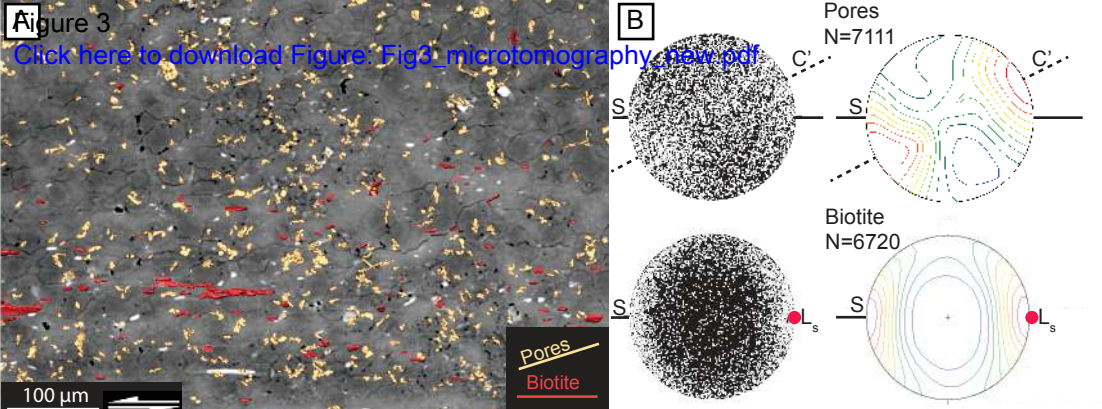

Fig. 3

Figure 4

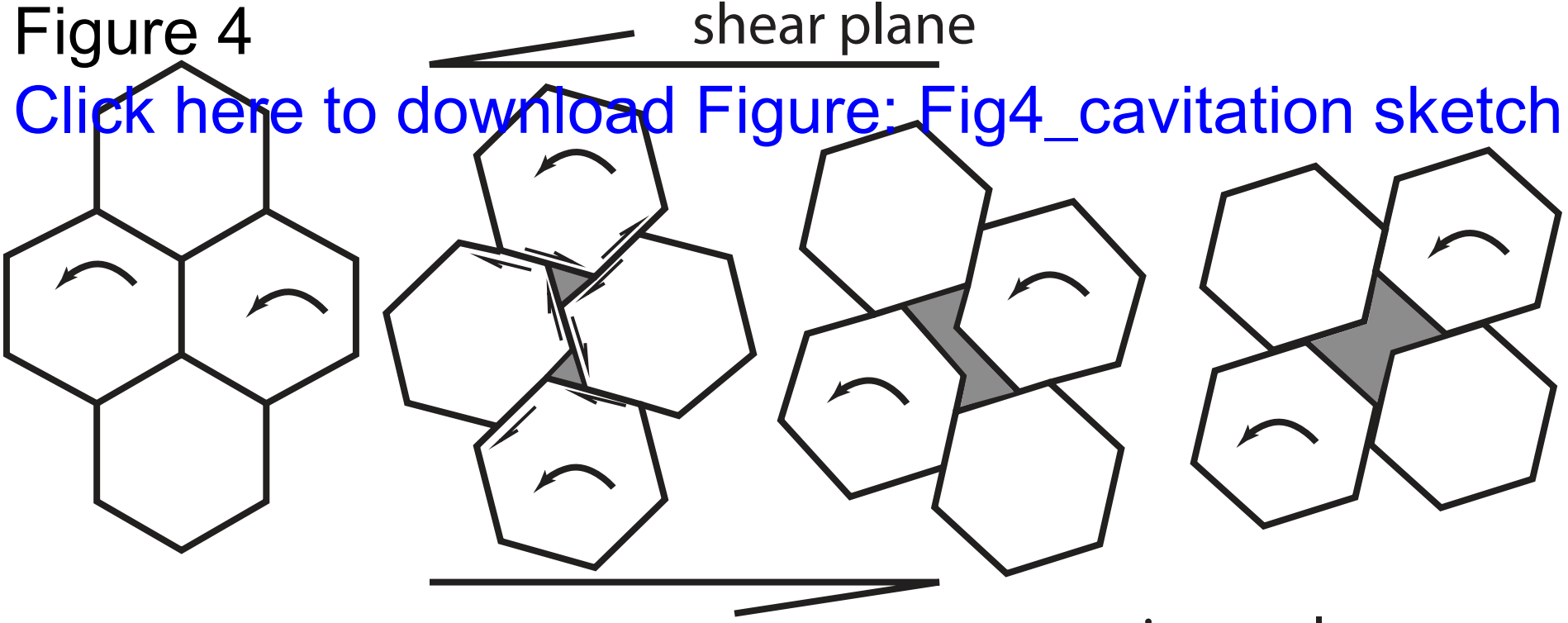

SUPPLEMENTARY MATERIALS

Methods

Light- and Scanning Electron Microscopy. The petrography and microstructure of the ultramylonite have been investigated with polarized light- and scanning electron microscopy on polished thin sections cut perpendicular to the foliation and parallel to the stretching lineation. SEM backscatter electron images were collected with a Jeol-840 SEM at the Department of Medical Biology, University of Tromsø, and with a Philips XL-30 FEG-ESEM at the Department of Geological Sciences, Stockholm University. The same thin sections were used for electron backscattered diffraction (EBSD). The grain size and aspect ratio of individual grains were measured on grain boundary maps obtained from manually digitizing SEM-BSE and EBSD images. The 2D size of the grains was calculated as the diameter of the circle with an area equivalent to that of the grain using the freeware Image SXM software (http://www.ImageSXM.org.uk).

EBSD and EDS Analysis. EBSD and EDS analysis were carried out on a Jeol LV6610 SEM equipped with an Oxford Instruments Nordlys Nano EBSD detector and with an Oxford Instruments SDD X-Max 80 mm^2 EDS detector at the Electron Microscopy Centre of Plymouth University. Additional EBSD analysis was conducted on a Philips XL-30 FEG-ESEM equipped with a HKL Technology (Oxford Instruments) Nordlys detector at the Department of Geological Sciences, Stockholm University. Thin sections were chemically polished carbon coated (for EBSD analysis in Plymouth) or left uncoated (for the EBSD analysis in Stockholm) during the acquisition of the electron backscatter patterns over gridded areas of varying sizes. Step sizes of 1, 2 and 3 μm were used in the 3 EBSD datasets presented in this study. Working conditions during the pattern acquisition were 20 or 25 keV accelerating voltage and either low vacuum (0.3-0.4 torr: Stockholm) or high vacuum (Plymouth). EBSD patterns were indexed and processed with the Channel 5 analysis suite from HKL Technology (Oxford Instruments). A match unit for oligoclase was created with the Twist component of the Channel 5 suite using the cell parameters for An16 (spatial group C-1) reported in Phillips et al. (1971) and served as theoretical model to index plagioclase. Noise reduction on the raw EBSD data was performed following the procedure tested by Prior et al. (2002) and Bestmann and Prior (2003). Crystallographic data were plotted on pole figures (upper hemispheres) using one point per grain.

X-Ray Microtomography. Microtomographic samples with a diameter of 1 mm were extracted from the ultramylonite sample shown in Fig. DR1B using a rock drill. These samples were scanned at the microtomography beamline 2BM of the Advanced Photon Source (USA). A double multilayer monochromator of 1.5% band- width provided 27 KeV X-rays; radiographic projections were collected in transmission mode by a CCD camera behind the sample in the hutch configuration. The sample detector distance was 70 mm. During each scan, 1440 projections were collected through rotating the samples in steps of 0.125° over 180°. The acquisition time for each data set was about 25 min. From the radiographic projections, three-dimensional absorption microtomography datasets were reconstructed using filtered back-projection.

Two microtomographic data-sets (Lu-1_light and Lu-3_light) were cropped to a volume of 1000x1000x750 voxels, which corresponds to 650x650x488 μm. From these subvolumes, pores, which are the least-attenuating, hence darkest phase in the data, were segmented by binary thresholding. From the same raw data, micas were segmented using the same algorithm. Biotite was chosen because it defines the mylonitic foliation in the sample. From the segmented mica data artefacts (mostly phase contrast 'shadows') had to be manually removed. Binary data of both the pores and the micas were sequentially loaded into Blob3D (Ketcham, 2005) for analysis. Blob3D recognises face-connected voxels of the same kind as clusters (or 'blobs'), which allows determining for each cluster the volume, shape, location and orientation (given in direction cosine of the inscribed eigenvectors), amongst other parameters. For our orientation analysis, all clusters smaller than 34 μm^3 (125 voxels) and larger than 4120 μm^3 (15000 voxels) were discarded. The former would have introduced artefacts due to the limited possibilities to arrange a small number of voxels in a pore cluster, and the latter would have very complex shapes, producing meaningless results. We furthermore discarded pore clusters with aspect ratios ≤ 1.7 and mica clusters with aspect ratios < 3. The orientation values of the longest eigenvector were converted into dip direction/dip angle values using the formulation given in Groshong (2006).

For each of the two datasets (Lu-1_light and Lu-3_light), two orientation datasets exist – one for the mica grains and one for the pores. The longest eigenvectors of both mica data-sets cluster around well-defined maxima. We assume these maxima to define the orientation of the longest diameter of the finite strain ellipsoid in each sample. As can be seen in the supplementary movies and also Fig. 3A, the mica furthermore define a mylonitic foliation. We used these two orientations as a kinematic framework. Because this framework does not

spatially coincide with the Cartesian coordinate axes of the microtomography data, we rotated the maximum defined by the longest eigenvectors of the mica data into a horizontal E-W orientation and the pole to the foliation in a horizontal N-S orientation using Stereo32 (Fig. 3A and DR2). The exact same rotations were then applied to the longest eigenvectors of the Lu-3_light and Lu-1_light pore populations, which yield the stereo plots shown in Fig. 3B and DR2. This allowed us to assess the orientation of the pores in a kinematic context.

Whole-Rock Chemical Analysis. Whole-rock chemical analysis of major elements was performed by wavelength dispersive X-Ray fluorescence (WD-XRF) analysis with a Bruker S8 Tiger XRF spectrometer at the Department of Geology, University of Tromsø. Powder samples were mixed and diluted at 1:7 with $Li_2B_4O_7$ flux, and melted into fused beads. Loss on ignition (LOI) was determined from weight lost after ignition at 1050°C for 1.5 h. Total Carbon (TC) was measured with a LECO CS-200 at the Department of Geology, University of Tromsø. The LECO CS-200 uses infrared absorption to measure the quantity of carbon dioxide generated by combustion of the sample in an induction furnace in a pure oxygen environment. Accuracy of the measurements is ± 2 ppm.

Supplementary Information on the Mass-Balance Calculations

The two samples were collected along a continuous strain gradient in the field at a relative distance of 1 meter, so that we can safely conclude that the ultramylonite derives from (micro)structural and mineralogical modifications of the monzonite. The mass-balance calculations were carried out following the method designed by Potdevin and Marquer (1987), which is referred to as the 'normalized Gresens' method. The method uses the following equation to derive mass gain or loss of a chemical component n during modification of rock A to rock B in relationship to the initial amount of the component n in rock A:

$$\Delta X_n = F_v\,(\rho_B/\rho_A)(X_{nB}/X_{nA}) - 1 \qquad (1)$$

ΔXn represents the gain or loss of chemical component n related to its initial content in rock A, F_v is the volume factor (F_v = V modified rock B/V initial rock A), X_{nA} is the weight % of the component n in the initial rock A, X_{nB} is the weight % of the component n in the modified rock B, ρ_A is the density of the initial rock A, and ρ_B is the density of the modified rock B. Our calculations refer to the transformation protolith → ultramylonite (sample LST29F → sample LST29B). The main differences are in the LOI and TC content, consistent with fluid infiltration during shear zone formation. The very minor difference between the compositions

of the monzonite and ultramylonite (Table DR1) indicate that, apart form the fluid infiltration, there has been no major chemical change during deformation. Our whole-rock chemical composition data are consistent with the average composition of the Raftsund mangerite (Griffin et al. 1978). Thus, we are confident that primary heterogeneities of the protolith do not represent a limitation to our analysis.

The density of the samples have been measured with a pycnometer using pulverized material at the Department of Geology, University of Tromsø, following routine procedures outlined in Hutchinson (1975). Weight measurements were repeated 5 times for each sample, and were reproducible with an accuracy of ± 0.004 grams. The densities of the protolith (monzonite) and of the ultramylonite are 2.711 g/cm^3 and 2.654 g/cm^3, respectively.

Setting ΔX_n for TC = 2.75 and solving (1) for F_v, we obtain F_v = 1.023. This means a 2.3% volume increase. Setting F_v = 1.023 and solving (1) for ΔXn, we derive the following gains or losses of chemical components:

	F_v	ΔXn
SiO_2	1.023	0.0150
Al_2O_3	1.023	0.0264
TiO_2	1.023	- 0.2642
Cr_2O_3	1.023	- 0.3932
Fe_2O_3	1.023	- 0.1644
MnO	1.023	0.1133
MgO	1.023	- 0.1416
CaO	1.023	- 0.0991
Na_2O	1.023	0.1741
K_2O	1.023	- 0.1472
P_2O_5	1.023	- 0.2025
LOI	1.023	1.7635
TC	1.023	2.7500

REFERENCES CITED

Bestmann, M., and Prior, D.J., 2003, Intragranular dynamic recrystallization in naturally deformed calcite marble: diffusion accommodated grain boundary sliding as a result of subgrain rotation recrystallization: Journal of Structural Geology, v. 25, p. 1597-1613.

Griffin, W.L., Taylor, P.N., Hakkinen, J.W., Heier, K.S., Iden, I.K., Krogh, E.J., Malm, O., Olsen, K.I., Ormaasen, D.E., and Tveten, E., 1978, Archaean and Proterozoic crustal

evolution in Lofoten-Vesterålen, N Norway: Journal of the Geological Society [London], v. 135, p. 629-647.

Groshong, R.H., 2008, 3D Structural Geology - A practical guide to quantitative surface and subsurface map interpretation. Springer, 400 pp.

Hutchinson, C.S., 1975, Laboratory handbook of petrographic techniques: Wiley, New York, 527 p.

Ketcham, R.A., 2005, Computational methods for quantitative analysis of three-dimensional features in geological specimens: Geosphere, v. 1, p. 32-41.

Phillips, M.V., Colville, A.A., and Ribbe, P.H., 1971, The crystal structures of two oligoclases: a comparison with low and high albite: Zeitschrift für Kristallographie, v. 133, p. 43-65.

Potdevin, J.L., and Marquer, D., 1987, Méthodes de quantification des transferts de matière par les fluides dans les roches métamorphiques déformées: Geodinamica Acta, v. 1, p. 193-206.

Prior, D.J., Wheeler, J., Peruzzo, L., Spiess, R., and Storey, C., 2002, Some garnet microstructures: an illustration of the potential of orientation maps and misorientation analysis in microstructural studies: Journal of Structural Geology, v. 24, p. 999-1011.

Table DR1. Whole-rock chemical composition (major elements) of the protolith (LST29F) and of the ultramylonite (LST29B) samples used for the mass-balance calculations.

Label	**LST29F**	**LST29B**
Rock Type	Undeformed Monzonite	Ultramylonite
SiO_2	58.61	58.97
Al_2O_3	18.67	18.99
TiO_2	1.04	0.76
Cr_2O_3	0.01	0.01
Fe_2O_3	5.24	4.34
MnO	0.09	0.10
MgO	0.98	0.84
CaO	3.86	3.45
Na_2O	5.19	6.04
K_2O	4.72	3.99
P_2O_5	0.49	0.39
Total	98.90	97.86
LOI	0.207	0.567
TC	0.037	0.138

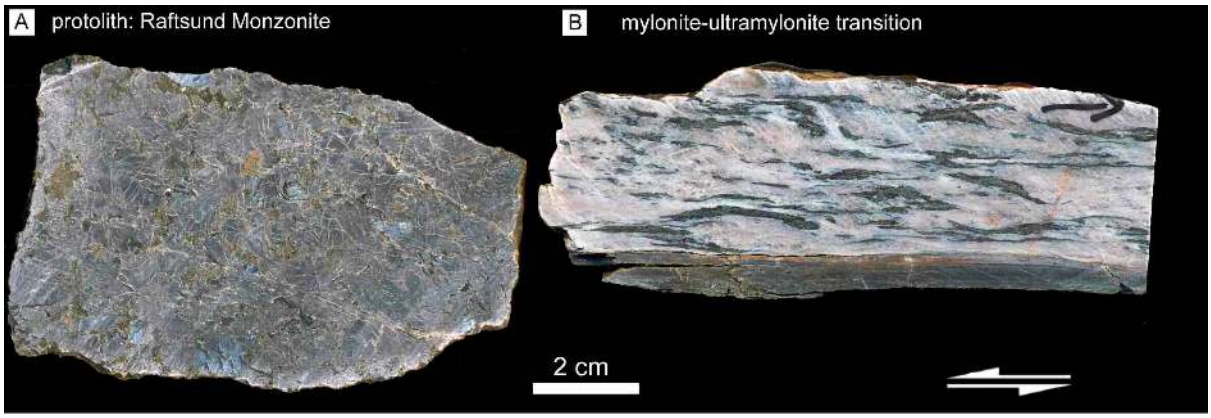

Figure DR1. Hand specimens of the monzonite protolith (A) and of the mylonite-ultramylonite transition (B).

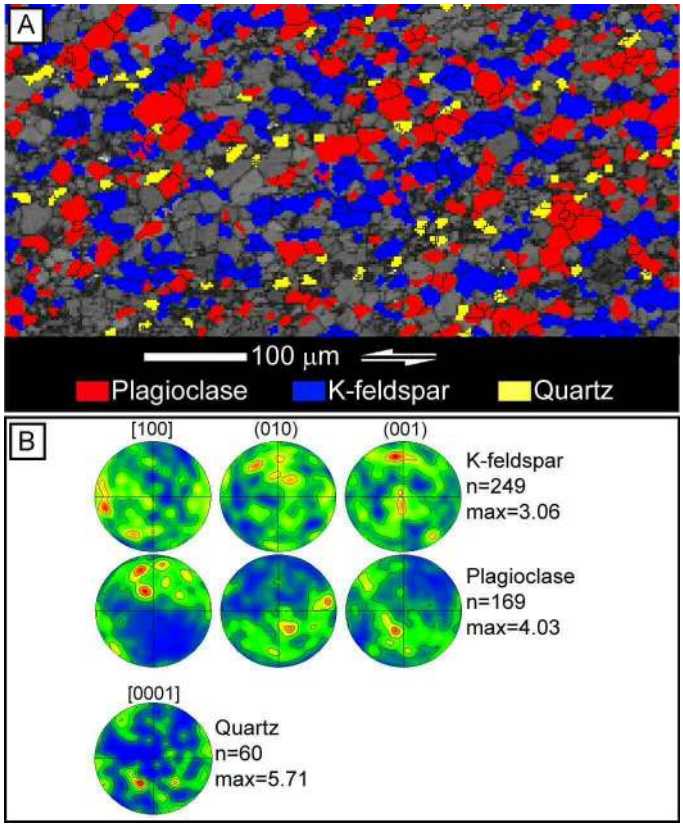

Figure DR2. A: EBSD-derived phase map of part of the same feldspathic layer shown in Fig. 2A of the paper. Note the festoons of quartz grains with a C'-band orientation for a sinistral sense of shear. B: Pole figures of K-feldspar, plagioclase and quartz grains in A.

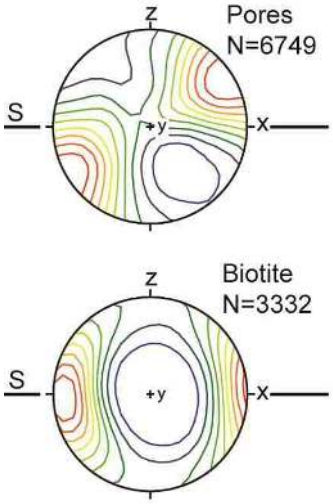

Figure DR3. Synchrotron x-ray microtomographic data Lu-1_light (compare with Fig. 3B). S is the trace of the ultramylonite foliation, Z is the pole to the foliation, X is parallel to the stretching lineation. Pole figure illustrating the long axes of pores preferentially oriented at 20-30° to the foliation (top) and the preferred orientation of biotite long axis aligned in the

foliation plane (bottom). Equal area lower hemisphere stereoplots. Contouring is up to 10 times MUD.

Movie DR_Lu-1_pores_slcmigration. Migrating slice through the microtomographic data-set Lu-1_light (volume of 650x650x488 μm). Grey values correspond to x-ray absorption. See text for further details.

Movie DR_Lu-3_pores_slcmigration. Thick migrating slice through the microtomographic data-set Lu-3_light (volume of 650x650x488 μm). Grey values correspond to x-ray absorption. Red=biotite, yellow=pores. The greyscale image is the backside of a thin migrating box through the 3D data-set, in which pores and biotite are highlighted. As the box moves through the volume, pores and biotite disappear out of the box at the front and enter the slice at the back, through the greyscale image See text for further details.

Movie file 1 (supplemental file)
Click here to download Movie File: DR_Lu-1_light_pores_slcmigration.mpg

Movie File 2 (supplemental file)
Click here to download Movie File: DR_Lu-3_light_pores_slcmigration.mpg